Intracellular pH dynamics respond to extracellular matrix stiffening and mediate vasculogenic mimicry through β-catenin

Running Title: Stiff matrix lowers pH, inducing cancer phenotypes

Leah M. Lund[1,2], Angelina N. Marchi[1,2,5], Laura Alderfer[3,6], Eva Hall[3], Jacob Hammer[1,2], Riley Moremen[1,2], Ijeoma Asilebo[1,2], Keelan J. Trull[1,2,7], Donny Hanjaya-Putra[2,3,4] and Katharine A. White[1,2*]

[1]Department of Chemistry and Biochemistry, University of Notre Dame
251 Nieuwland Science Hall
Notre Dame, IN 46556 USA

[2]Harper Cancer Research Institute, University of Notre Dame
1234 N. Notre Dame Avenue
South Bend, IN 46617 USA

[3]Bioengineering Graduate Program, Aerospace and Mechanical Engineering, University of Notre Dame
2010G McCourtney Hall East
Notre Dame, IN 46556 USA

[4]Chemical and Biomolecular Engineering, University of Notre Dame
250 Nieuwland Hall
Notre Dame, IN 46556 USA

[5]Current: Siemens Healthineers
430 S Beiger St.
Mishawaka, IN 46544

[6]Current: Vivodyne
Suite 775 601 Walnut Street
Philadelphia PA 19106 USA

[7]Current: Lander University
231 Stanley Ave
Greenwood, SC 29649

*Corresponding author. Email: kwhite6@nd.edu Telephone: 574.631.9962
A128 Harper Hall
1234 N. Notre Dame Avenue
South Bend, IN 46617

Competing Interests: Authors declare no competing interests.

Abstract

Dysregulated intracellular pH (pHi) dynamics and an altered tumor microenvironment have emerged as drivers of cancer cell phenotypes. However, the molecular integration between the physical properties of the microenvironment and dynamic intracellular signaling responses remains unclear. Here, we identify a mechanistic link between ECM stiffness and pHi dynamics in driving vasculogenic mimicry (VM), an aggressive cancer phenotype associated with poor prognosis. We performed single-cell imaging of pHi in lung and breast metastatic cell lines cultured on tunable-stiffness hydrogel systems. We used two tunable-stiffness hydrogel systems to independently model stiffness induced by increased protein secretion (Matrigel) and increased protein crosslinking (Hyaluronic acid gels). We show that increased ECM stiffness lowers single-cell pHi in both lung and breast metastatic cell lines. We also observed that stiff ECM promotes a distinct morphological phenotype called vasculogenic mimicry (VM). Importantly, we show that low pHi is a necessary mediator of VM, as raising pHi on stiff ECM reduces VM phenotypes. We also find that lowering pHi on soft ECM was sufficient to induce VM in the absence of extracellular stiffening. We characterized β-catenin as a pH-dependent molecular mediator of VM, where stiffness-driven increases in β-catenin abundance can be overridden by high pHi, which destabilizes β-catenin to reduce VM on stiff ECM. In contrast, the transcription factor FOXC2 is activated by ECM stiffness but is insensitive to pHi, and its activity alone is insufficient to maintain VM at high pHi when β-catenin is lost. We uncover a novel mechanotransduction axis in which ECM stiffness regulates intracellular pH to drive β-catenin-induced VM. We also show pHi dynamics can override mechanosensitive cell responses to the extracellular microenvironment. Thus,

our work positions pHi as an integrator of mechanotransduction in cancer, suggesting a new framework for therapeutically targeting pHi in cancer and perhaps in other diseases driven by ECM remodeling.

Introduction

The extracellular matrix (ECM) is a protein-rich structure that becomes dysregulated in cancer, driving cancer cell adaptation and the promotion of cancer cell phenotypes[1]. This increasingly rigid and dense tumor ECM promotes cancer cell invasion and vasculogenic mimicry, an adaptive cancer phenotype [2,3]. In addition to the dysregulated extracellular environment, cancer cells also experience dysregulated pH dynamics[4], with increased intracellular pH (pHi) (>7.4) and decreased extracellular pH (pHe) (<7.2) compared to normal epithelial cells (pHi 7.0-7.3; pHe 7.4)[5]. This reversal of the pH gradient is an early event in cellular transformation[6] and has been directly linked to adaptive changes in cancer cell signaling, metabolism, proliferation, and evasion of apoptosis[5].

Increased ECM stiffness promotes various cancer cell phenotypes including increased hypoxia[7], vasculogenic mimicry[8], cell durotaxis[9], and selection for tumor-initiating cells or cancer stem-cell phenotypes[4,10–13]. Importantly, many equivalent or similar processes are also linked to dysregulated pHi dynamics, including hypoxia[11], cell invasion[4], and maintenance of a stem-like phenotype in adult and embryonic stem cell models[14]. However, the molecular mechanisms that integrate the physical properties of the microenvironment with intracellular cancer cell signaling are largely unknown.

90 While prior work has shown pHi dynamics can directly regulate normal
91 mechanosensitive behaviors including focal adhesion remodeling[15] and epithelial cell-
92 cell contacts[16,17], there are significant gaps in knowledge of the molecular crosstalk
93 between ECM stiffening and pHi dynamics in cancer cells. One limitation is technical: it
94 is challenging to develop mechanically tunable model systems that mimic physiological
95 ECM dysregulation with suitable control. Previous studies have used synthetic ECM
96 models, including Matrigel/Geltrex-[18] and Hyaluronan-based[19] systems. However, these
97 studies have not decoupled the contributions of ECM protein abundance and ECM
98 crosslinking density as independent drivers of mechanosensitive cell responses.
99 Another limiting factor in characterizing molecular links between ECM stiffness
100 and pHi is that most mechanistic studies of pHi dynamics are performed under non-
101 physiological culture conditions and lack single-cell resolution. These limitations are
102 compounded when the goal is to explore effects of physical forces on cellular pHi
103 dynamics and in the context of phenotypically heterogeneous cancer cells.
104 Here, we pair synthetic tunable-stiffness ECM models with live-cell pHi
105 measurements and non-invasive pHi manipulation approaches to elucidate how pHi
106 dynamics respond to ECM stiffening. We further explore the mechanistic role of pHi in
107 regulating a cancer-associated mechanosensitive phenotype called vasculogenic
108 mimicry (VM). We use two synthetic matrix models to mimic ECM stiffening through
109 increasing protein abundance (Matrigel/Geltrex) and crosslinking density (hyaluronic
110 acid gels), and measure single-cell pHi in metastatic breast and lung cancer cells. We
111 show that pHi decreases with increased stiffness using both matrix models. We also
112 demonstrate that cells plated on stiff ECM acquire distinct VM phenotypes that can be

113 modulated by dynamically altering pHi. Importantly, raising pHi in cells plated on stiff
114 matrix reduces VM phenotypes while lowering pHi in cells plated on soft matrix induces
115 acquisition of a VM phenotype. We also investigate the pH dependence of two
116 molecular regulators of VM (β-catenin and FOXC2). We show that β-catenin is a pH-
117 dependent mediator of VM phenotype while FOXC2 activity is pH-insensitive. This
118 suggests β-catenin as a necessary regulator of pH-dependent vasculogenic mimicry.
119 Overall, our work reveals a previously unidentified link between mechanosensing and
120 pHi dynamics in cancer and further suggests low pHi as a necessary and sufficient
121 mediator of VM, a phenotype associated with aggressive cancers.
122

123 **Results**

124 **Stiffening extracellular matrix lowers pHi in metastatic human lung carcinoma**

125 Increased tumor microenvironment (TME) stiffness (>1000 Pa) can be caused by
126 increased ECM protein deposition or by increased crosslinking of the ECM proteins
127 compared to normal epithelial ECM (50-100 Pa)[20] (**Figure 1A**). To investigate the
128 central hypothesis of how a stiffening extracellular environment alters pHi, we used two
129 tunable-stiffness hydrogel models to control ECM stiffness with high specificity. To
130 mimic the effects of ECM stiffness changes resulting from altered ECM protein
131 crosslinking, we used a hyaluronic-acid (HA) gel system where variable crosslinking
132 density tunes ECM stiffness independently of protein concentration or composition[21,22].
133 HA is a non-sulfated linear polysaccharide of (1-β-4)d-glucuronic acid and (1-β-3)N-
134 acetyl-d-glucosamine, and is a ubiquitous component of the ECM[19]. HA is abundant in

135 the extracellular environment of the lung and brain[19], and increased HA secretion is
136 associated with cancer[19] and fibrotic diseases of the liver and lung[23].
137 Recent work has shown that HA can be functionalized to contain thiol-reactive
138 cross-linkable regions, with high crosslinking adding rigidity to the ECM, enabling
139 tunable stiffness[24]. Our HA gel tunable-stiffness model consists of a uniform
140 concentration and mixture of gelatin and thiol-modified hyaluronan across stiffnesses,
141 while stiffness is controlled by modulating amounts (%) of thiol-reactive PEGDA
142 crosslinker (see methods for details). The HA gel model consists of four levels of
143 crosslinking agent mimicking ECM stiffness changes induced by increased protein
144 crosslinking and has a previously reported tunable stiffness range from ~100-1500 Pa[25]
145 (**Figure 1B**). This system allows us to modulate matrix stiffness by adjusting the extent
146 of ECM protein crosslinking while maintaining a consistent concentration of matrix
147 components (hyaluronan and gelatin) across all stiffness conditions. This enables
148 modeling ECM stiffness effects independently of matrix concentration changes.
149 To mimic the effects of stiffness changes induced by increased ECM protein
150 secretion, we used Matrigel- or Geltrex-based tunable-stiffness gel systems. Matrigel
151 and Geltrex are naturally-derived matrices that mimic the tumor microenvironment of
152 stromal-rich tissues, such as breast, lung, and prostate[26]. The Matrigel and Geltrex
153 commercial matrix mixtures are rich in laminin and collagen, ECM proteins that directly
154 promote integrin signaling[27]. Varying the concentration of Matrigel and Geltrex
155 effectively titrates ECM protein concentrations[28], mimicking ECM stiffening caused by
156 the increased secretion of ECM proteins[29]. We generated tunable-stiffness
157 Matrigel/Geltrex models using four Matrigel/Geltrex concentrations (4 mg/mL-12 mg/mL)

158 with stiffness ranges of ~50-1,500 Pa[30–32] (**Figure 1B**). For these stiffness
159 determinations, the manufacturer reports a shear modulus (*G'*) that can be converted to
160 Young's modulus (matrix stiffness) using the following equation E= 2*G*'(1 + *v*). Prior
161 work has indicated that hydrogels can be assumed to be incompressible[33,34], such that
162 their Poisson's ratio (*v*) approaches 0.5, simplifying the equation to E=3*G*'. Importantly,
163 in the Matrigel/Geltrex tunable-stiffness gel systems, as the ECM protein concentrations
164 increase, so does the available ligand concentration for integrin-mediated interactions.
165 This gel model allows the assessment of ECM stiffening on pHi when intracellular
166 integrin signaling is also titrating.

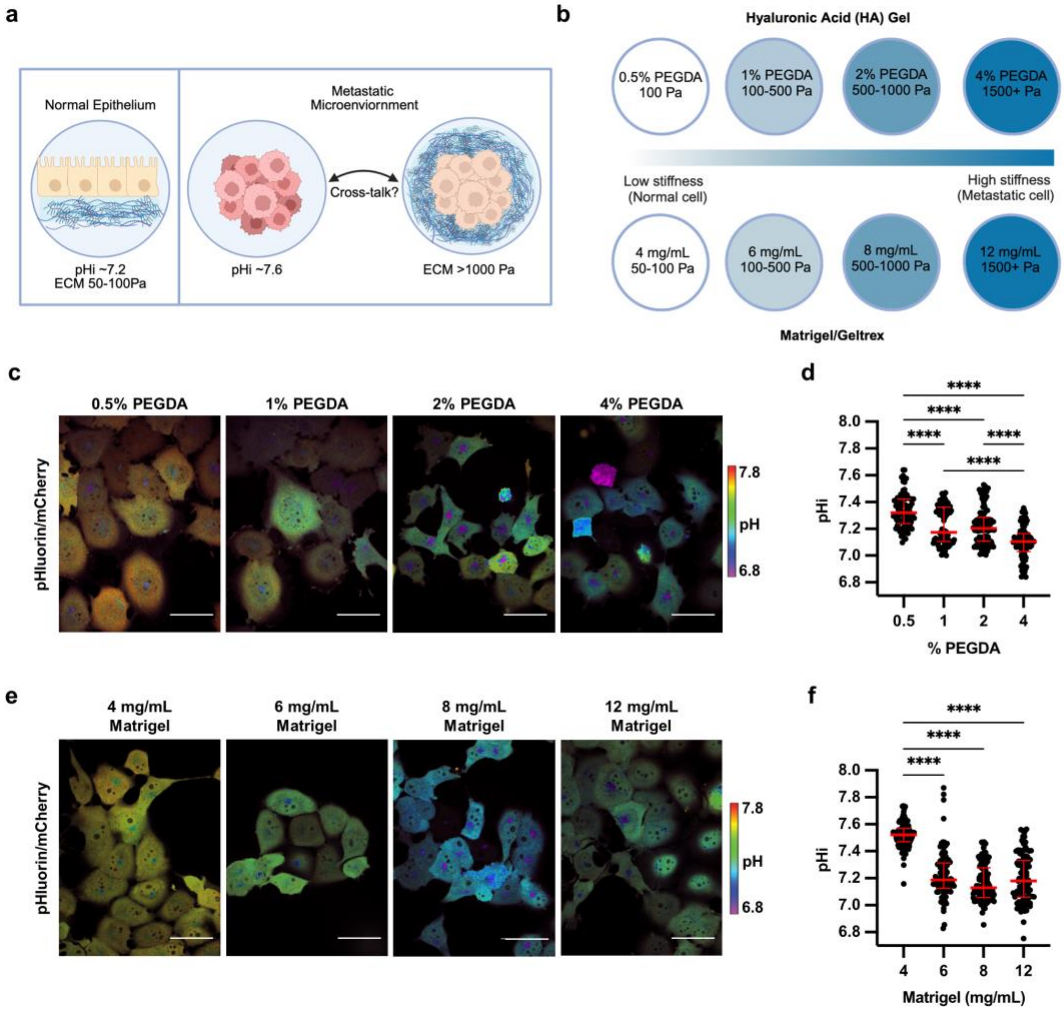

167

168 **Figure 1: Stiffening extracellular matrix lowers pHi in metastatic human lung**
169 **carcinoma (H1299). a)** Schematic of increased pHi and ECM stiffening (via increased
170 protein secretion and increased protein crosslinking) associated with tumorigenesis. **b)**
171 Schematic of synthetic ECM models with tunable-stiffness (~50 Pa-1,500 Pa). The
172 Matrigel (or Geltrex) model mimics increased ECM protein secretion while hyaluronic
173 acid (HA) gel system mimics increased ECM protein crosslinking. **c)** Representative
174 images of H1299 cells stably expressing mCherry-pHluorin pH biosensor plated on
175 varying HA gel stiffnesses. Images show ratiometric display of pHluorin/mCherry
176 fluorescence. Scale bars: 50 µm. **d)** Quantification of single-cell pHi data collected as
177 shown in (c). (n=3 biological replicates; n=91 0.5% PEGDA, n=90 1% PEGDA, n=102
178 2% PEGDA, n=89 4% PEGDA. Red lines show medians ± IQR). **e)** Representative
179 images of H1299 cells stably expressing mCherry-pHluorin pH biosensor plated on
180 varying Matrigel stiffnesses. Images show ratiometric display of pHluorin/mCherry
181 fluorescence. Scale bars: 50 µm. **f)** Quantification of single-cell pHi data collected as
182 shown in (e). (n=3 biological replicates; n=93 4mg/mL, n=92 6mg/mL, n=102 8mg/mL,
183 n=97 12mg/mL. Red lines show medians ± IQR). For (d) and (f), significance was
184 determined by a Kruskal-Wallis test (****P<0.0001).
185

186 With the two tunable-stiffness hydrogel systems established, we next selected
187 cancer cell lines that originated from tissues with a relatively soft ECM, such as lung
188 and breast, where tumorigenic ECM stiffening has been associated with both increased
189 metastasis and invasion[26]. We have previously established and characterized single-cell
190 pHi heterogeneity in a clonal metastatic lung cancer cell line (H1299) and a clonal
191 breast cancer cell line (MDA-MB-231), all plated and imaged on glass[35]. We have
192 engineered these cell lines to stably express a genetically-encoded ratiometric pH
193 biosensor mCherry-pHluorin (mCh-pHl)[35]. This biosensor is a fusion of the fluorescent
194 protein pHluorin (pKa 7.1) that is pH-sensitive in the physiological range, and the
195 fluorescent protein mCherry, that is pH-insensitive in the physiological range[36]. For
196 accurate pHi measurements in single cells, ratiometric imaging of pHluorin and mCherry
197 fluorescence can be performed followed by single-cell standardization using isotonic
198 buffers with a known pH containing the protonophore Nigericin to equilibrate intracellular
199 and extracellular (buffer) pH[37]. Single-cell standard curves are then generated, enabling

200 back-calculation of pHi from pHluorin and mCherry fluorescence intensity ratios (**Figure**
201 **S1**, see methods for details). This biosensor has successfully been used in prior studies
202 to measure single-cell spatiotemporal pHi dynamics in clonal cancer and normal
203 epithelial cell populations without affecting cell morphology or behavior[15,35,36].
204 To determine the effects of altered ECM stiffness on pHi, we cultured H1299
205 cells expressing the mCh-pHl biosensor on matrix-coated imaging dishes for 48 hours.
206 This incubation allowed for cells to adhere and respond to the varied stiffness of each
207 matrix system. In cells plated on HA gels, single-cell pHi decreased with increasing
208 stiffness (**Figure 1C**). Cells plated on the stiffest matrix (4% PEGDA) had significantly
209 decreased pHi (**Figure 1D**; 7.10±0.07; median±interquartile range (IQR)) compared to
210 cells on the softest matrix (0.5% PEGDA) (**Figure 1D**; 7.32±0.10; median±IQR). We
211 also observed that intermediate ECM stiffnesses (1% PEGDA and 2% PEGDA)
212 produced intermediate pHi values, with a stepwise trend of decreasing pHi with
213 increasing stiffness (**Figure 1D**; 2% PEGDA 7.20±0.10; 1% PEGDA 7.17±0.19;
214 medians±IQR). The overall decrease in pHi of ~0.2 pH units between soft and stiff ECM
215 is within the range of physiological pHi dynamics shown to regulate normal cell
216 behaviors, including cell cycle progression[35], differentiation[13,38], and migration[39]. This
217 result demonstrates that ECM stiffening through changes in protein crosslinking drives
218 significant decreases in single-cell pHi of clonal metastatic lung cancer cells. These
219 data suggest that progressive changes in ECM stiffness within the physiological range
220 of normal to metastatic mechanical stiffness environments can alter pHi in metastatic
221 cancer cells, suggesting a potential role for pHi in mechanosensitive cancer cell
222 signaling and behaviors.

223 We next determined whether the stiff ECM decreased pHi using the Matrigel
224 tunable-stiffness models, where ECM protein concentration is the predominant driver of
225 altered stiffness. In cells plated on varied Matrigel stiffnesses, single-cell pHi decreased
226 with increasing stiffness (**Figure 1E**). Cells plated on the stiffest matrix (12 mg/mL) had
227 a significantly decreased pHi (**Figure 1F**; 7.18±0.15; median±IQR) compared to the
228 softest matrix (**Figure 1F**; 4 mg/mL; 7.52±0.49; median±IQR). The decrease in pHi of
229 ~0.35 units between stiffest (~1,500 Pa) and softest (~50 Pa) ECM in this system is also
230 consistent with the pHi changes measured between stiffest and softest HA gel models
231 (~0.22 units). However, in the Matrigel tunable-stiffness model system, the pHi of cells
232 measured on intermediate stiffnesses (**Figure 1F**; 6 mg/mL Matrigel, 7.19±0.13; 8
233 mg/mL Matrigel, 7.13±0.14; medians±IQR) was not significantly different from the pHi of
234 cells plated on a stiff matrix, suggesting that in the context of titrating integrin signaling,
235 the effect may be more binary compared to stiffness changes induced by crosslinking.
236 These results show that ECM stiffening lowers pHi in metastatic cells regardless of
237 whether the stiffness change is induced by increased ECM protein abundance or ECM
238 protein crosslinking.
239 We next confirmed that increased ECM stiffness decreases pHi using another
240 metastatic breast cell model (MDA-MB-231), which is also derived from a stromal-rich
241 environment (like H1299). We found that the pHi of MDA-MB-231 cells was decreased
242 by ~0.2 units in cells plated on a stiff matrix compared to soft matrix in both the HA gel
243 (soft 7.43±0.14; stiff 7.28±0.10; medians±IQR) (**Figure S2A, B**) and the Matrigel (soft
244 7.40±0.14; stiff 7.20±0.13; medians±IQR) models (**Figure S2 C,D**). Again, with the HA
245 gel model, we observed step-wise effects of pHi in response to stiffness with

246 intermediate pHi values on the intermediate stiffnesses (**Figure S2B**), just as we saw
247 with the metastatic lung model (**Figure 1C,D**). While the pHi of MDA-MB-231 cells was
248 significantly decreased on stiff (12 mg/mL) compared to the softest (4 mg/mL), the pHi
249 response of MDA-MB-231 on the intermediate stiffnesses was more variable on
250 Matrigel (**Figure S2D**). While we cannot rule out that pHi response to ECM may vary
251 depending on cell type or matrix composition, we predict that these discrepancies are
252 due instead to cell-line dependent responses to the very low integrin ligand
253 concentration when using the lowest dilution (4 mg/mL) of Matrigel/Geltrex. When using
254 the HA-gel system, where protein concentration is maintained across stiffnesses, the
255 behavior of H1299 and MDA-MB-231 are in close concordance.

256 Both H1299 and MDA-MB-231 are derived from soft tissue (breast and lung) and
257 were isolated from soft metastatic sites (lymph node and pleural effusion). To determine
258 whether metastatic cells from a stiff tissue of origin are similarly sensitive to ECM
259 stiffening, we cultured metastatic bone cancer cells (U-2 OS) on soft and stiff HA gels.
260 We found that these cells similarly had reduced pHi when cultured on stiff ECM
261 compared to soft (**Figure S3**, 0.5% PEGDA. 7.28±0.09; 4% PEGDA 7.15±0.05;
262 medians±IQR). This matched relationship of pHi and ECM stiffness in metastatic cells
263 derived from both soft and stiff tissues suggest that decreased pHi may be a conserved
264 metastatic cell response to ECM stiffening.

265 Taken together, these data show that increased ECM stiffness mediated by
266 either increased crosslinking (HA gel model) or by increased ECM protein secretion
267 (Matrigel model) decreases pHi of metastatic cancer cells. Our data also show that the
268 stiffness-dependent decreases in pHi are not tissue-specific, as both breast and lung

269 metastatic models exhibited lower pHi on stiff compared to soft matrices. In summary,
270 these data demonstrate an inverse relationship between ECM stiffening and pHi in
271 metastatic cell models and suggest a role for pHi in cell responses to mechanical ECM
272 cues.

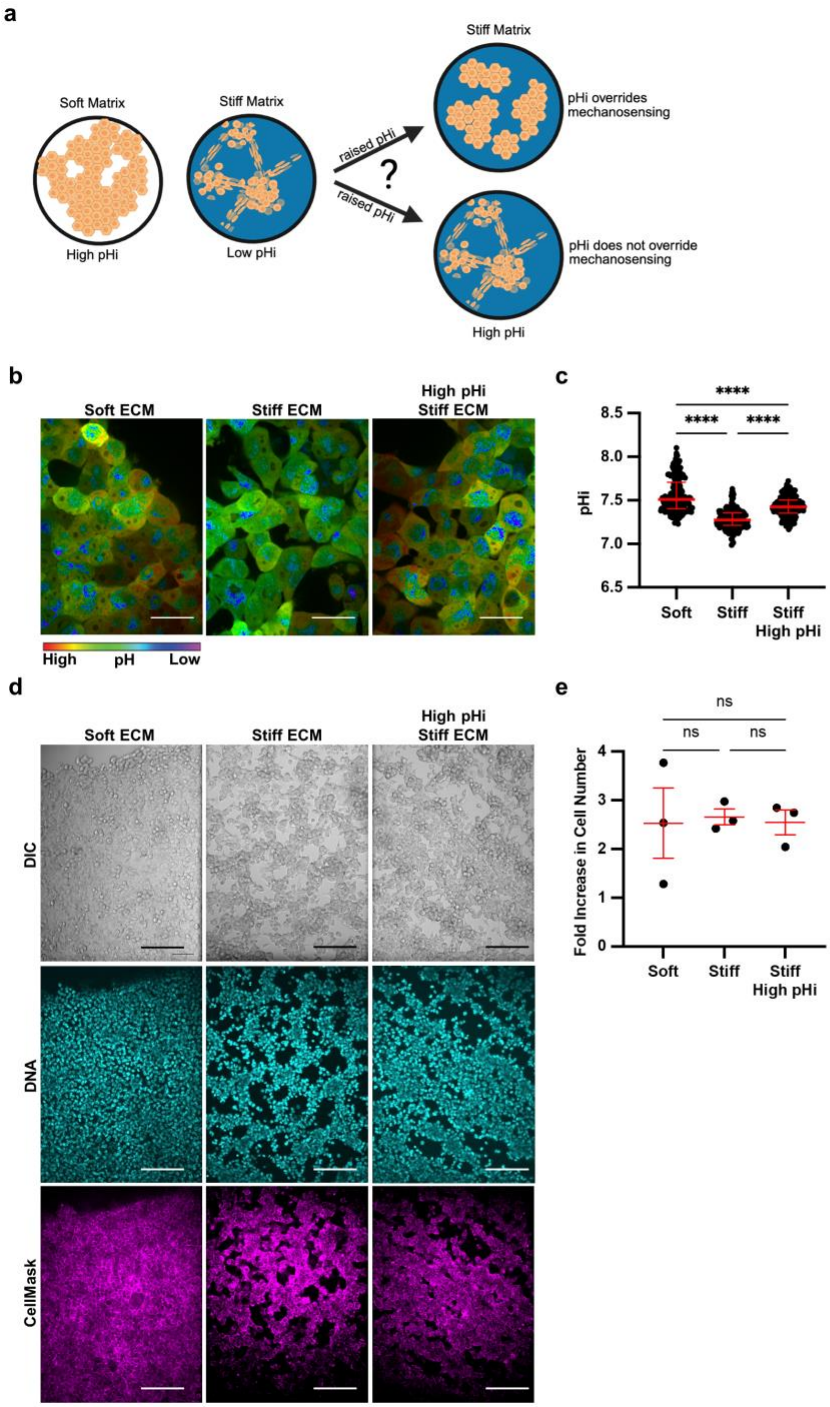

Figure 2: Stiffness-dependent vasculogenic mimicry is reduced when pHi is increased on stiff ECM. a) Schematic of vasculogenic mimicry (VM) in 2D on stiffening matrix. **b)** Representative images of H1299 cells stably expressing mCherry-pHluorin pH biosensor plated on soft (0.5% PEGDA) and stiff (4% PEGDA) HA gels and stiff (4% PEGDA) with raised pHi (culture media supplementation with 50mM sodium

279 bicarbonate). Images show ratiometric display of pHluorin/mCherry fluorescence ratios.
280 Scale bars: 50 μm. **c)** Quantification of single-cell pHi data collected as shown in (b)
281 (n=3 biological replicates; n=201 soft, n=237 stiff, n=239 stiff high pHi. Red lines show
282 medians ± IQR). **d)** Representative images of H1299 cells plated on soft (0.5% PEGDA)
283 and stiff (4% PEGDA) HA gels. Images show differential interference contrast (DIC) and
284 Hoechst stain (DNA, cyan). Scale bars: 100 μm. **e)** Quantification of cell proliferation
285 across manipulation conditions. (n=3 biological replicates. Red lines show means ±
286 SEM).
287

288 **Stiffness-dependent vasculogenic mimicry is reduced in high pHi conditions in**
289 **metastatic cell models**

290 When performing single-cell pHi measurements, we also observed a distinct
291 change in overall cancer cell morphology that correlated with increased ECM stiffness.
292 Metastatic cancer cells plated on soft matrix grew in flat lawns of cobblestone (H1299)
293 or spindle-shaped cells (MDA-MB-231), forming a near-confluent sheet. However, on
294 stiff matrix, the metastatic cancer cells grew in compact clusters of irregularly shaped
295 cells, frequently exhibited 3D growth phenotypes, and formed connected bridges of
296 elongated spindle shaped cells between 3D "nodes" (**Figure S4**). Similar changes in cell
297 morphology are found in vasculogenic mimicry (VM), an aggressive cancer phenotype
298 observed both *in vivo* and *in vitro*, where tumor cell organize into vessel-like structures,
299 allowing nutrients and oxygen access independent of traditional angiogenesis[40].
300 Previous studies have shown that increased ECM stiffness drives VM[41] phenotypes and
301 characterized 2D VM phenotypes as a growth pattern where cells form distinct networks
302 of tightly packed cells with surrounding open space devoid of cell growth[42].
303 Our data show stiff ECM lowers single-cell pHi and induces VM phenotypes,
304 leading to the hypothesis that low pHi is a necessary mediator of VM (**Figure 2A**). If this
305 hypothesis is correct, raising pHi in cells plated on stiff matrix should reduce the VM

306 phenotype (**Figure 2A**). To directly test this hypothesis, we established protocols to
307 experimentally raise pHi in cells plated on stiff ECM. Prior work showed that 50 mM
308 sodium bicarbonate supplemented into the media for 24 hours was sufficient to raise
309 pHi in H1299 cells plated on glass[35]. We imaged single-cell pHi in H1299 cells plated on
310 soft ECM, stiff ECM, and stiff ECM with bicarbonate supplementation to raise pHi
311 (**Figure 2B**). We found that bicarbonate significantly increased pHi of cells plated on
312 stiff ECM compared to untreated cells on stiff matrix (stiff 7.27±0.08; stiff + Bicarbonate
313 7.43±0.08; medians±IQR) (**Figure 2C).** The bicarbonate treatment increased the pHi of
314 cells plated on the stiffest ECM by approximately 0.2 pH units (**Figure 2C**), which is
315 similar to the magnitude of pHi changes we observed between soft and stiff ECM across
316 the various cell lines and gel systems.
317 We next tested the effects of increased pHi on the stiffness-dependent
318 vasculogenic mimicry phenotype. We found that H1299 cells acquired a vasculogenic
319 mimicry phenotype on stiff matrix, and this VM phenotype was abrogated when pHi was
320 increased (**Figure 2D**). Cells plated on stiff matrix with bicarbonate-induced increases in
321 pHi grew in a 2D cobblestone-like morphology similar to that of cells grown on soft ECM
322 (**Figure 2D**, additional representative images in **Figure S4**). To confirm that the
323 observed pH-dependent changes in cell morphology were not due to differences in cell
324 proliferation, we assayed proliferation rates in H1299 cells plated on soft and stiff ECM
325 with and without increased pHi. Importantly, we did not observe any significant
326 differences in proliferation rates across our experimental conditions over the timeframe
327 tested (**Figure 2E**).

328 To quantify the observed stiffness- and pHi-dependent changes in cell
329 morphology, we used a cell membrane marker and quantitative image analysis pipeline
330 (see methods for details) to assess cell area (**Figure 3A**). Notably, single-cell area of
331 H1299 cells was significantly lower in cells plated on stiff ECM compared to soft ECM
332 (Figure 3B; stiff 339 μm^2±189; soft 407 μm^2±225; medians±IQR). This result
333 demonstrates that cell area is a robust quantitative indicator that decreases with the
334 acquisition of VM morphology phenotype on stiff ECM. This allows us to quantitatively
335 distinguish cell morphologies corresponding to low VM and high VM using cell area.
336 Importantly, we found that cell area significantly increased (**Figure 3B**; 374 μm^2±193;
337 median±IQR) when pHi was raised in H1299 cells plated on stiff ECM compared to
338 control H1299 on stiff ECM (**Figure 3B**). This indicates that increased pHi significantly
339 reduces the stiffness-dependent VM phenotype. The loss of VM networks and
340 increased cell area when pHi is raised on stiff ECM demonstrates that low pHi is
341 required for cells to maintain VM on stiff ECM.
342 We also probed the VM phenotype in MDA-MB-231 cells and U-2 OS cells and
343 found that single-cell area of both MDA-MB-231 (**Figure S5**) and U-2 OS cells (**Figure**
344 **S6**) was decreased in cells plated on stiff ECM compared to soft. Raising pHi in MDA-
345 MB-231 cells on stiff ECM did produce a noticeable shift in morphology, reverting cells
346 to the flatter, spread morphology observed on soft ECM (**Figure S5C**) and when we
347 quantified cell area we found a trend toward increased cell size, though it was not
348 statistically significantly different from stiff (**Figure S5D**, p=0.2549). However, MDA-MB-
349 231 cells already have pronounced mesenchymal-like phenotype which may obscure
350 these cell area calculations (reducing the measurable dynamic range). These findings

351 demonstrate that while high pHi can reverse stiffness-induced VM in metastatic cells,
352 inherent mesenchymal traits of some metastatic cells like MDA-MB-231 may limit the
353 extent to which VM-associated morphological change can be measured. Together, our
354 findings confirm that vasculogenic mimicry is an ECM stiffness-mediated phenotype and
355 further identify decreased pHi as a previously unrecognized necessary regulator of VM
356 phenotypes.

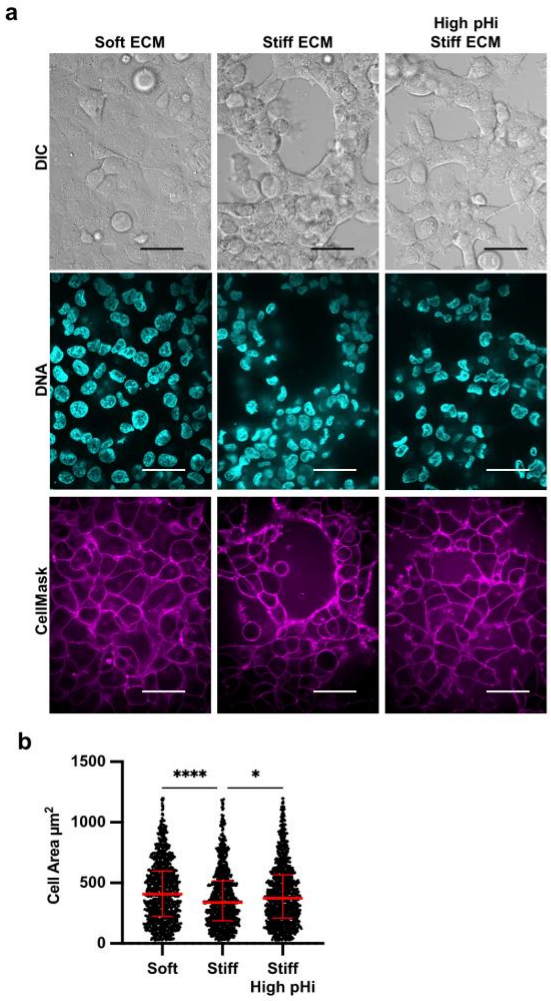

357
358 **Figure 3: Vasculogenic mimicry phenotype decreases cell area on stiff ECM,**
359 **which is rescued by increasing pHi in metastatic lung carcinoma. a)**
360 Representative images of H1299 cells plated on soft (0.5% PEGDA) and stiff (4%
361 PEGDA) HA gels and stiff (4% PEGDA) with raised pHi. Images show differential
362 interference contrast (DIC), Hoechst 33342 (DNA, cyan) and CellMask Deep Red
363 membrane stain (Cy5, magenta). Scale bars: 50 µm. **b)** Quantification of single-cell area

364 collected as shown in (a) (n=3 biological replicates, n=1061 soft, n=954 stiff, n=1078
365 stiff high pHi. Red lines show medians ± IQR).
366

367 **β-catenin abundance is stiffness-dependent, pHi-dependent, and necessary for**
368 **stiffness-dependent vasculogenic mimicry**

369 We next investigated molecular drivers of pH-dependent regulation of VM. In
370 epithelial cells, VM is regulated by several mechanisms, including the activity and
371 abundance of β-catenin[43,44], a multifunctional protein that regulates cell-cell adhesion
372 and transcription, and the activity of transcription factor FOXC2[42,45]. These two
373 molecular regulators of VM have previously characterized pH-sensitive activity in
374 epithelial models (β-catenin)[17,46] or *in vitro* (FOXC2)[47]. However, existing literature is
375 conflicting as to whether FOXC2 and β-catenin are truly independent drivers of VM. For
376 example, prior data suggests that β-catenin functions upstream of FOXC2 in VM, with
377 β-catenin directly controlling expression of FOX transcription factors[48]. However, other
378 data suggests that FOXC2 can itself modulate Wnt signaling[49,50] and rescue acquisition
379 of vasculogenic mimicry when β-catenin levels are reduced[48]. We next used our models
380 to differentiate roles of FOXC2 and β-catenin in regulating stiffness- and pH-dependent
381 VM phenotypes.

382 While FOXC2 has been shown to be required for VM[45], and sufficient to drive
383 endothelial cell vascularization[48], it is unclear whether FOXC2 abundance or activity is a
384 sufficient driver of VM phenotypes. We first measured FOXC2 abundance in H1299
385 cells plated on soft ECM and stiff ECM and found no difference in FOXC2 expression
386 (**Figure S7A,B**), indicating FOXC2 protein abundance is not regulated by stiffness or
387 pHi. We next measured FOXC2 transcriptional activity in single cells using a FOXC2

388 transcriptional activity reporter plasmid (FOXC2-TAG-Puro) that has FOXC2 specific
389 tandem repeats flanking a core DNA binding element upstream of GFP (LipExoGen,
390 see methods) (**Figure S7C**). We found that FOXC2 activity was significantly increased
391 in cells plated on stiff ECM compared to cells plated on soft ECM (**Figure S7D)**,
392 suggesting that ECM stiffening is sufficient to increase FOXC2 transcriptional activity.
393 However, FOXC2 transcriptional activity remained high when pHi was increased on a
394 stiff matrix (**Figure S7**), suggesting pHi is not a sufficient modulator of FOXC2 activity in
395 this model. Furthermore, our data show that high FOXC2 transcriptional activation is not
396 a sufficient driver of VM in this model, as high pHi abrogates VM phenotypes (**Figure**
397 **2&3**) even as FOXC2 activity remains high (**Figure S7**).
398 We next tested the hypothesis that stiffness-associated pHi dynamics modulate
399 VM by regulating β-catenin abundance in metastatic cancer cell lines. Previous work
400 has shown that β-catenin abundance and transcriptional activity directly regulate VM[43].
401 Furthermore, increased β-catenin nuclear localization correlates with VM formation in
402 colon cancer models[44] and is associated with ECM stiffening in liver cancer models[51].
403 Importantly, ECM stiffening has also been shown to increase whole-cell β-catenin
404 abundance in some cell lines, including human mesenchymal stem cells[52,53]. Work from
405 our lab has also shown that pHi can directly regulate β-catenin stability in normal
406 epithelial cells, with high pHi reducing β-catenin stability while low pHi stabilizes β-
407 catenin and increases its adhesion and transcriptional activity[17]. However, our prior
408 work did not assess pH-dependent β-catenin stability in non-epithelial models and did
409 not fully characterize the functional consequences of pH-dependent β-catenin stability
410 on cell behaviors.

411 While previous studies have demonstrated the role of β-catenin in regulating VM,
412 these studies have not characterized the cellular cues by which a stiff ECM increases β-
413 catenin abundance or nuclear localization. To determine the effect of ECM stiffening on
414 β-catenin abundance, we performed immunofluorescent staining of β-catenin in H1299
415 cells plated on soft ECM and stiff ECM with and without pHi manipulation (**Figure 4A**).
416 We found that both whole-cell and nuclear β-catenin abundance were significantly
417 increased in cells plated on stiff ECM (low pHi) compared to cells plated on soft ECM
418 (high pHi) (**Figure 4B,C**). This is in agreement with our prior work showing that low pHi
419 stabilizes β-catenin in epithelial cells[53]. Furthermore, we found that when we raised pHi
420 in cells plated on stiff ECM, VM was reduced, and whole-cell and nuclear β-catenin
421 abundance was significantly reduced compared to control cells plated on stiff ECM
422 (**Figure 4B,C**). We also confirmed these results in the MDA-MB-231 model, showing
423 that low pHi on stiff ECM increases β-catenin whole cell and nuclear abundance
424 compared to soft, and that raising pHi on stiff ECM reduces β-catenin abundance
425 (**Figure S8**). Thus, our data demonstrate that increased β-catenin abundance is
426 correlated with low pHi in human metastatic cancer cells. Taken together, these data
427 suggest that pH-dependent β-catenin abundance underlies the observed pH-dependent
428 regulation of VM. Finally, these data show that high pHi can override mechanosensing
429 by decreasing β-catenin abundance, suggesting that low pHi functions as a necessary
430 mediator of VM in cancer cells via stabilization of β-catenin.

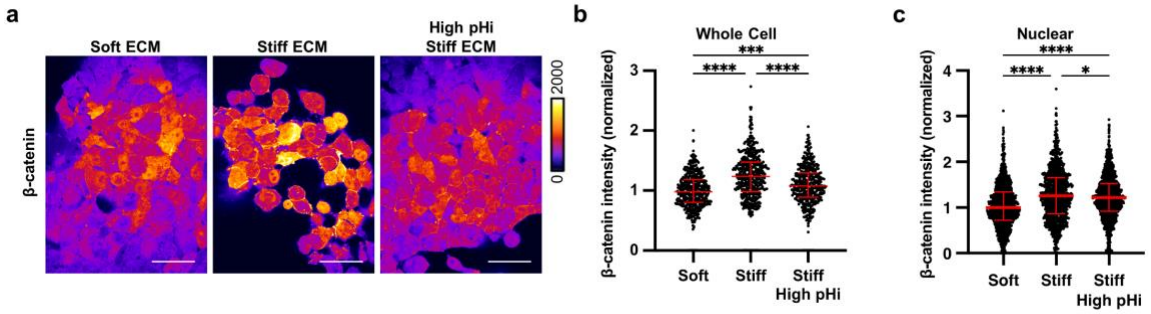

Figure 4: Increased pHi reduces β-catenin abundance and nuclear localization in stiff matrix conditions. a) Representative images of H1299 cells plated on soft (0.5% PEGDA), stiff (4% PEGDA) and stiff with raised pHi (4% PEGDA) HA gels fixed and stained for β-catenin. β-catenin is pseudocolored according to scale. Scale bars: 50 μm. **b)** Quantification of whole cell β-catenin intensity collected as shown in (a). (n=3 biological replicates, n=452 soft, n=486 stiff, n=415 stiff high pHi. Red lines show medians ± IQR). **c)** Quantification of nuclear β-catenin intensity collected as described in (a). (n=3 biological replicates, n=1043 soft, n=975 stiff, n=1157 stiff high. Red lines show medians ± IQR). For (b) and (c), significance was determined by a Kruskal-Wallis test (**P*<0.05; ***P*<0.01; ****P*<0. 001; *****P*<0.0001).

We next asked whether stabilizing β-catenin at high pHi could rescue VM on stiff ECM. To test this, we stabilized β-catenin abundance in high pHi conditions using CHIR, an inhibitor of GSK-3β, a required component of the β-catenin destruction complex[54]. We confirmed that CHIR treatment does not disrupt the previously characterized stiffness-dependent and treatment-dependent pHi dynamics in H1299 lung cancer models (**Figure 5A**). Again, we observed reduced β-catenin on stiff ECM when pHi was raised, but CHIR supplementation to this condition significantly increased β-catenin abundance (**Figure 5B,C**). Furthermore, we found that when treated with the CHIR inhibitor, cells with raised pHi on a stiff matrix exhibited an increase in vascular mimicry. (**Figure 5D,E**). This data suggests that rescuing β-catenin abundance under high pHi conditions rescues VM on stiff ECM, and further demonstrates β-catenin as a primary regulator of pH-dependent VM in this model. Combined with our FOXC2 results,

455 our data also show that β-catenin loss at high pHi regulates VM independently of

456 FOXC2 activity, reducing VM phenotypes even while FOXC2 transcriptional activity

457 remains high.

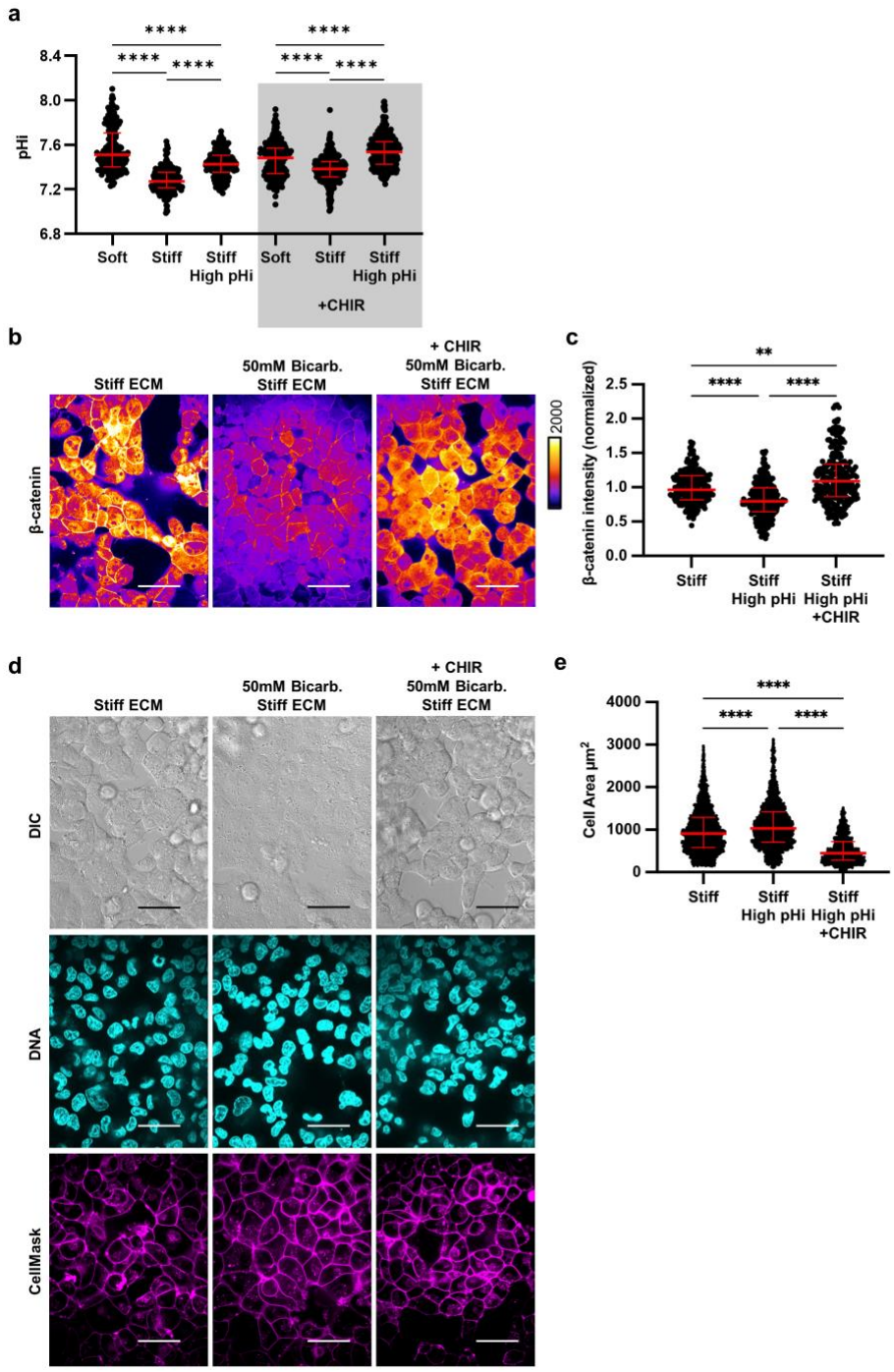

458

459 **Figure 5: Stabilization of β-catenin abundance under high pHi rescues VM on a**
460 **stiff matrix. a)** Quantification of pHi data from parental H1299 cells and H1299 cells
461 treated with CHIR treatment with and without treatment with sodium bicarbonate
462 (Bicarb.) (see methods) (n=3 biological replicates. n=191 soft, n=219 stiff, n=198 stiff
463 high pHi, n=302 soft +CHIR, n=373 stiff +CHIR, n=408 stiff high pHi +CHIR. Red lines
464 show means ± SEM). **b)** Representative images of H1299 cells plated on stiff HA gels
465 (4% PEGDA) with and without raised pHi (Bicarb.) and with or without CHIR treatment
466 fixed and stained for β-catenin. β-catenin is pseudocolored according to scale. Scale
467 bars: 50 μm. **c**) Quantification of whole cell β-catenin intensity collected as shown in (b).
468 (n=3 biological replicates, n=452 stiff, n=486 stiff high pHi, n=415 stiff high pHi +CHIR.
469 Red lines show medians ± IQR). **d)** Representative images of H1299 cells plated on stiff
470 HA gels (4% PEGDA) with and without raised pHi (Bicarb.) and with or without CHIR
471 treatment. Images show differential interference contrast (DIC), Hoechst 33342 (DNA,
472 cyan) and CellMask Deep Red membrane stain (Cy5, magenta). Scale bars: 50 μm. **e)**
473 Quantification of single-cell area collected as shown in (d) (n=3 biological replicates,
474 n=452 stiff, n=486 stiff high pHi, n=415 stiff high pHi +CHIR. Red lines show medians ±
475 IQR).
476

477 **Low pHi is a sufficient driver of vasculogenic mimicry phenotypes on soft ECM**

478 The prior results suggest that low pHi is necessary for VM on stiff ECM, as
479 raising pHi can override stiffness-associated VM phenotypes. We next hypothesized
480 that low pHi is a sufficient mediator of VM and that lowering pHi in H1299 cells plated on
481 soft matrix can induce stiffness-independent acquisition of VM phenotypes. To directly
482 test this hypothesis, we used an H1299 cell line deficient in the sodium proton
483 exchanger (H1299-NHE1 K.O., see methods). We performed an acid load recovery
484 assay to confirm that the H1299-NHE1 K.O. cell line had no measurable NHE1 activity
485 (**Figure S9**). This H1299-NHE1 K.O. cell line has significantly decreased basal pHi
486 compared to parental H1299, and bicarbonate treatment raised pHi in this model
487 (**Figure 6A**). Using this experimental system, we tested the effects of decreased pHi on
488 modulating VM phenotypes. We found that the H1299-NHE1 K.O. cells acquired a VM
489 phenotype on soft matrix, suggesting low pHi is indeed a sufficient driver of VM in the
490 absence of stiff ECM mechanical cues (**Figure 6B**). Importantly, the stiffness-

491 independent VM phenotype observed in H1299-NHE1 K.O. cells on soft ECM was
492 again reduced when pHi was raised in cells on the soft matrix (**Figure 6B**). We used cell
493 area to quantify the extent of VM phenotype and found that when pHi is lowered
494 (H1299-NHE1 K.O.) in cells plated on soft ECM, single-cell area is significantly
495 decreased compared to when pHi was raised in the same cells plated on soft ECM
496 (**Figure 6C,D**). Our findings demonstrate that decreased pHi is sufficient to drive a VM
497 phenotype in the absence of stiffening ECM mechanical cues. We confirm in this model
498 that increasing pHi is sufficient to override VM phenotypes, even when VM is aberrantly
499 generated on soft ECM.

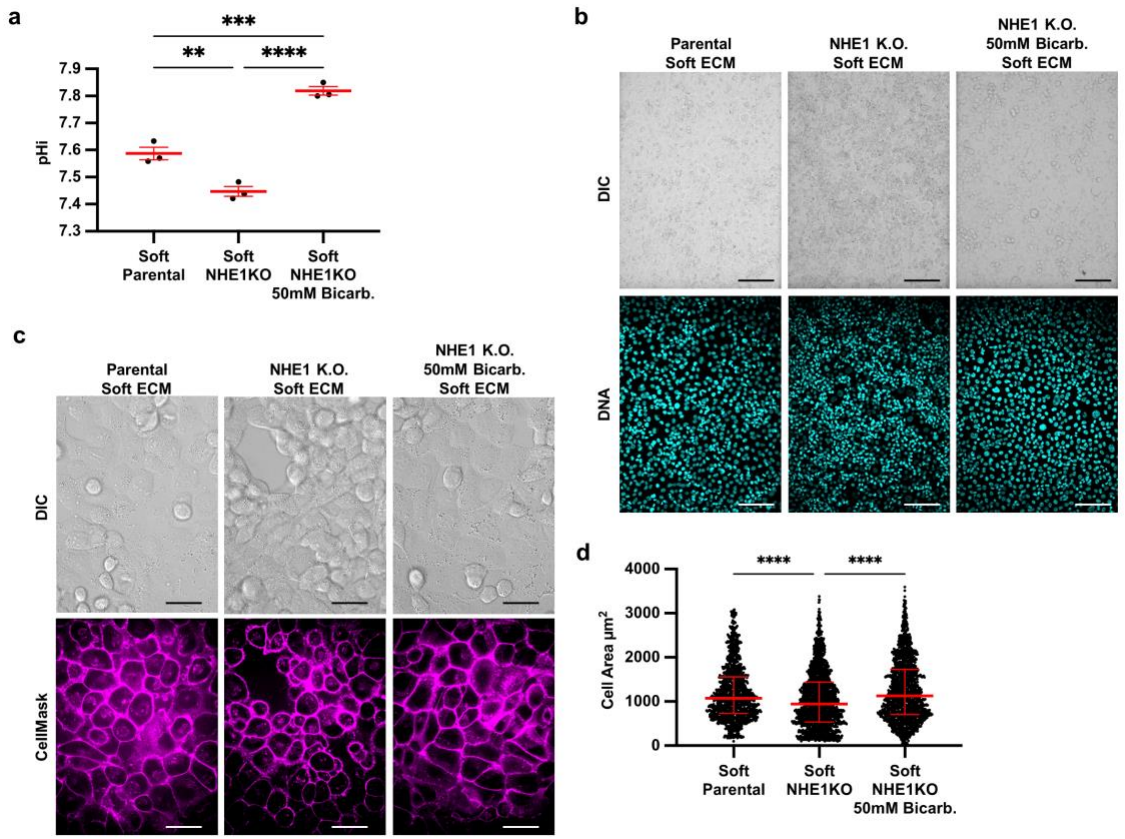

500

501 **Figure 6: Low pHi is sufficient to induce vasculogenic mimicry on a soft ECM. a)**
502 Quantification of pHi data from parental H1299 cells and H1299 cells where NHE1
503 knockout via CRISPR (H1299-NHE1 K.O.). with and without treatment with sodium

504 bicarbonate (Bicarb.) (see methods) (n=3 biological replicates. Red lines show means ±
505 SEM). **b)** Representative images of H1299 cells plated on soft HA gels (0.5% PEGDA)
506 with and without lowered pHi (H1299-NHE1 K.O.) and with or without increased pHi
507 (H1299-NHE1 K.O. Bicarb.). Images show differential interference contrast (DIC) and
508 Hoechst 33342 (DNA, cyan). Scale bars: 100 µm. **c)** Representative images of H1299
509 cells plated on soft HA gels (0.5% PEGDA) with and without lowered pHi (H1299-NHE1
510 K.O.) and with or without increased pHi (H1299-NHE1 K.O. Bicarb.). Images show
511 differential interference contrast (DIC) and CellMask Deep Red membrane stain (Cy5,
512 magenta). Scale bars: 50 µm. **d)** Quantification of single-cell area collected as shown in
513 (a) (n=3 biological replicates, n=383 parental, n=267 NHE1 K.O., n=315 NHE1 K.O.
514 Bicarb. Red lines show medians ± IQR).
515

516 **Discussion**

517 Our work identifies pHi dynamics as a previously unrecognized regulator of
518 stiffness-dependent VM in metastatic cancer cell models. We combined physiologically
519 relevant tunable-stiffness hydrogel systems with single-cell pHi imaging and quantitative
520 microscopy approaches to reveal novel molecular integration of the extracellular
521 mechanical environment and pHi. We show that increasing ECM stiffness, driven by
522 either increased protein concentration or crosslinking, lowers the single-cell pHi of lung,
523 breast, and bone cancer cell lines. Most previously described tumorigenic behaviors
524 such as hyperplasia[55], metastatic progression[35,56], and drug resistance[56] are
525 associated with increased pHi. However, recent work suggests a potential role for
526 comparatively low cancer cell pHi in regulating hypoxia response[57] and modulating
527 tumor initiating cell phenotypes[14]. Adding to these recent data, our new findings show
528 that low pHi in cancer cells is both a necessary and sufficient driver of VM. When we
529 raise pHi in cells plated on stiff ECM, we attenuate VM phenotypes, overriding
530 mechanosensitive regulation of VM. More surprisingly, low pHi was sufficient to drive
531 formation of VM phenotypes on soft ECM (in the absence of mechanical stiffening).

532 Our work characterizing pH-dependent molecular drivers of VM identified β-
533 catenin as a pH-sensitive regulator of vasculogenic mimicry. We also show that another
534 VM regulator, FOXC2, has stiffness-dependent but pHi-*independent* activity. Our
535 molecular characterization of VM regulators using tunable-stiffness hydrogels in
536 combination with pHi manipulation approaches also resolved conflicting data in the
537 literature on the interdependence of β-catenin and FOXC2 in VM regulation.
538 Importantly, our data suggest that β-catenin is a necessary regulator of stiffness-
539 dependent VM and that FOXC2 transcriptional activation is not sufficient to drive VM in
540 the absence of stabilized β-catenin.
541 Our data reveal that pHi is a master regulator of VM and can override
542 mechanosensitive phenotypes in 2D, improving understanding of molecular
543 mechanisms driving cancer cell adaptive behaviors in the context of a stiffening ECM. In
544 this work, we limit our characterization to 2D ECM models and a handful of metastatic
545 cell models while focusing on just one tumorigenic mechanosensitive phenotype (VM).
546 This approach enables us to combine quantitative single-cell pHi measurements and
547 pHi manipulation with tunable-stiffness hydrogel systems to differentiate the
548 contributions of stiffness and pHi in these complex cell morphology phenotypes. Our
549 findings provide the groundwork for future experiments investigating pHi-dependent
550 mechanosensitive behaviors in more complex 3D tumor spheroid models or even co-
551 culture models with cancer-associated fibroblasts or immune cells. Prior work has
552 already independently shown that complex 3D environments produce increased
553 vasculogenic mimicry and phenotypic heterogeneity[58] and pronounced pHi gradients[59].
554 Our current findings motivate expanding these studies to more complex mechanical and

555 cellular environments to explore mechanistic roles for pHi dynamics in regulating other
556 mechanosensitive tumorigenic behaviors such as durotaxis, invasion, and phenotypic
557 plasticity.
558
559 **Methods**
560 *Cell Culture*
561 H1299 (parental ATCC CRL-5803) or H1299-NHE1 K.O. (CRISPRed cell line was a gift
562 from Dr. Diane Barber at the University of California, San Francisco) were grown in
563 RPMI 1640 (Corning, 10-040-CV) supplemented with 10% Fetal Bovine Serum (FBS,
564 Peak Serum, PS-FB2). When using CHIR treatment (CHIR 99021, Ambeed, A133052),
565 10uM was supplemented to media 24 hours after plating.
566
567 MDA-MB-231 (ATCC HTB-26) cells were grown in DMEM (Corning, MT10013CVV)
568 supplemented with 10% FBS. All cells were maintained at 5% CO_2 and 37°C in a
569 humidified incubator. To increase pHi, cells were cultured under normal conditions for
570 24 hours before being treated for 24 hours with culture media supplemented to a final
571 concentration of 50-100mM Sodium Bicarbonate (Sigma-Aldrich; S6297-250G).
572
573 U2 OS (ATCC HTB-96) cells were grown in McCoy's 5A (Modified) Medium
574 (ThermoFisher Scientific; 16600082) supplemented with 10% FBS. All cells were
575 maintained at 5% CO_2 and 37°C in a humidified incubator.
576
577 *Transient Expression and Stable Cell Line Generation*

578 H1299 and MDA-MB-231 mCherry-pHluorin expressing cells were generated as
579 previously described[35]. FOXC2-TAG-Puro (LipExoGen Biotech, SKU:LTV-0061)
580 positive H1299 cells were generated using lentiviral article transduction. Briefly, H1299
581 cells were plated at 50% confluency in a 6 well tissue culture treated plate. After 24
582 hours, media was replaced with fresh media containing 10ug/mL of polybrene and
583 50uL/well of FOXC2-TAG-Puro lentiviral particles. Cells were incubated for 72 hours
584 prior to selection with 0.8 mg/mL blasticidin (Thermo Fisher Scientific, BP264725). After
585 4 weeks of selection, GFP positive cells were sorted on a BD FACS ARIA III cell sorter
586 using 488nm excitation with 515nm-545nm emission filter. These cells were collected
587 into 1mL 1XPBS using high purity sort settings. Cells were then centrifuged and plated
588 in complete RPMI media with 0.8 mg/mL blasticidin.
589
590 *Preparation of tunable-stiffness hydrogels*
591 *Matrigel or Geltrex gel systems*
592 Matrigel (Corning 356231, Lot 9035003) or Geltrex (Gibco, A14132-02, add LOT)
593 coated plates were made in 35 mm diameter, 4-well (9.5 mm/well) glass bottom dishes
594 (Matsunami, D141400). Stock Matrigel or Geltrex (12 or 16 mg/mL respectively) were
595 diluted in cold complete media to concentrations of 4 mg/mL, 6 mg/mL, and 8 mg/mL
596 which cover a range of stiffness from 50 Pa to ~1000 Pa[30–32]. Each well was coated with
597 2.6 µL matrix per mm of well surface area (25 µL/well for 9.5 mm 4-well plate). Matrix
598 was allowed to solidify at 37°C for 20 minutes prior to cell plating. Cells were plated at
599 5,000 cells per well in 100 µL solution volume.
600

601 *HA gel system*

602 HyStem-C (Advanced BioMatrix GS313) gels are composed of thiol-modified hyaluronic
603 acid (Glycosil, GS222F), thiol-modified gelatin (Gelin-S, GS231F), polyethylene glycol
604 diacrylate (PEGDA, Extralink, GS3007F), and degassed, deionized water (DG
605 Water)[22,30]. Basement matrix solution was made of 1:1 Glycosil and Gelin-S and varying
606 final PEGDA percentages (0.5, 1, 2, and 4%) were prepared in degassed, deionized
607 water. The basement matrix solution and respective percentage PEGDA were mixed in
608 a 4:1 parts ratio immediately before plating. Each well was coated with 1.4 µL matrix per
609 mm of well surface area (13.5 µL/well). Cells were plated on the pre-prepared synthetic
610 ECM plates 48 hours prior to imaging at 5,000 (single-cell pHi measurements) or 75,000
611 (VM imaging/staining) cells/well in 100 µL solution volume. HA gels were pre-prepared a
612 maximum of 3 days prior to plating of cells, and stored with Dulbecco's phosphate
613 buffered saline (DPBS) (Quality Biological, 114-057-101) in each well to maintain
614 hydration at 4°C.

615

616 *Microscope System*

617 Confocal images were collected on a Nikon Ti-2 spinning disk confocal with a 10x
618 (PLAN APO NA0.45) air objective, 40x (CFI PLAN FLUOR NA1.3) oil immersion
619 objective, and 60x (PLAN APO NA1.4) oil immersion objective. The microscope is
620 equipped with a stage-top incubator (Tokai Hit), a Yokogawa spinning disk confocal
621 head (CSU-X1), four laser lines (405 nm (100 mW), 488 nm (100 mW), 561 nm (100
622 mW), 640 nm (75 mW)), a Ti2-S-SE motorized stage, multi-point perfect focus system,
623 and an Orca Flash 4.0 CMOS camera. Images were acquired under the following

624 settings: pHluorin (GFP) (488 nm laser excitation, 525/36 nm emission), mCherry (561
625 nm laser excitation, 630/75 nm emission), Cy5 (647 nm laser excitation, 705/72 nm
626 emission), Hoechst 33342 Dye (405 nm laser excitation, 455/50 nm emission), TxRed
627 (561 nm laser excitation, 605/52 nm emission), and SNARF (561 nm laser excitation,
628 705/72 nm emission) and differential interference contrast (DIC) were used. Acquisition
629 times for each fluorescence channel ranged from 50-600 milliseconds.
630
631 *Single-cell pHi measurements using mCherry-pHluorin and confocal microscopy*
632 Prior to imaging, stage top incubator and microscope objectives were pre heated to
633 37°C and kept at 5% CO_2/95% air. Single-cell pHi measurements were performed as
634 previously described[35]. Briefly, initial fields of view (FOV) were collected on the cells in
635 their respective media. Two isotonic buffers (25 mM HEPES, 105 mM KCl, 1 mM $MgCl_2$)
636 were prepared and supplemented with 10 μM nigericin (Thermo Fisher Scientific,
637 N1495). For standardization, isotonic buffers were pre-warmed to 37°C and pH of the
638 "Nigericin buffers" was adjusted to ~6.7 and ~7.7 (with 1M KOH) (recorded for each
639 biological replicate to the hundredths place). For each standardization point, cells were
640 washed three times consecutively with no waiting time with appropriate Nigericin buffer
641 followed by a 5-7 minute equilibration prior to image acquisition. All required buffer
642 exchanges were carried out on the stage incubator to preserve XY positioning. Multiple
643 Z-planes were collected with the center focal plane maintained using the Perfect Focus
644 System (PFS).
645
646 *Single-cell pHi measurements using SNARF-AM and confocal microscopy*

647 U-2 OS cells were plated at $5x10^3$ cells per well (4-well glass bottom dish) in complete
648 medium 48 hours prior to imaging. Cells were treated for pHi manipulation as described
649 above. Cells were dye loaded in conditioned media with 10 μM of 5-(and-6)-Carboxy
650 SNARF™-1 Acetoxymethyl Ester, Acetate (Fisher Scientific, cat: C1272) prepared as a
651 100 μM stock solution dissolved in a 10% DMSO in DPBS for 15 minutes at 37°C and
652 5% CO_2. Dye-containing media was removed, and plates were washed three times for 5
653 min each time with pre-warmed complete growth medium containing appropriate
654 treatment. FOVs were selected by viewing cells in differential interference contract
655 (DIC). Images in SNARF (10% laser power, 400 ms), TxRed (30% laser power, 400
656 ms), and DIC (200 ms) channels for each FOV. SNARF dye was calibrated using three
657 pre-warmed Nigericin buffers (as described above).
658
659 *pHi Image Quantification*
660 NIS Analysis Software was used to quantify pHi. All images were background
661 subtracted using a region of interest (ROI) drawn on glass coverslip (determined by
662 DIC). Individual ROIs were drawn for each cell in each condition (initial, high pH
663 nigericin, and low pH nigericin). For each cell ROI, mean pixel intensities were
664 quantified and pHluorin/mCherry or SNARF/TxRed ratios were calculated in Microsoft
665 Excel. For each cell, the nigericin standard fluorescence intensity values were used to
666 generate single-cell standard curves where single-cell pHi was back-calculated based
667 on nigericin buffer pH values reported to the hundredths.
668
669 *Proliferation Assay*

670 H1299 cells were plated at 1,000 cells/well in a 24 well tissue-culture treated plate on
671 pre-prepared matrix (65 µL/well) (see *Preparation of tunable-stiffness hydrogels*). After
672 24 and 48 hours of culture, cells were lifted via trypsinization (0.25%, Corning, 25-
673 0530CI) for 20 minutes and counted by hemocytometer.
674
675 *Immunofluorescence Staining*
676 *Fixed Cell Staining*
677 H1299 and MDA-MB-231 cells were plated at 75,000 cells/well in 100 µL solution
678 volume on the pre-prepared synthetic ECM plates. After 48 hours, the media was
679 removed and a 3.7% Formaldehyde (Alfa Aesar, 50-000) solution in DPBS was added
680 to each well and allowed to fix at room temperature for 10 minutes. Cells were washed
681 3x2 minutes with DPBS before a permeabilization solution (0.1% Triton-X (Fisher
682 Scientific, 9002-93-1) in DPBS) was added to each well for ten minutes at room
683 temperature (RT). The Triton-X permeabilization solution was removed and cells were
684 washed 3x2 minutes with DPBS at RT before a blocking solution (1% BSA (Fisher
685 Scientific, BP1600-100) was added to cells for one hour at RT with rocking. The
686 blocking solution was removed and cells were washed 3x2 minutes with DPBS before
687 primary antibody solutions were added to each well and incubated with rocking at 4°C
688 overnight. Primary antibodies were prepared in 1% BSA with 0.1% Triton-X at 1:50
689 dilutions. Primary antibodies used were: β-catenin mouse (BD Biosciences,
690 BDB610154) Cyclin-D rabbit (Cell Signaling Technology, 55506S), and FOXC2 rabbit
691 (Cell Signaling Technology, 12974S). The following day, primary antibody solutions
692 were removed and cells were washed 3x2 minutes with DPBS before secondary

693 antibodies (Goat anti-mouse IgG (H+L) Cross-Absorbed Secondary Antibody, Alexa
694 Fluor 488; Invitrogen; A-11001, Goat anti-rabbit IgG (H+L) Secondary Antibody, Alexa
695 Fluor 488; Invitrogen; A-11008) were added at 1:1,000 in solution of 1% BSA, 0.1%
696 Triton-X, and Hoechst 33342 (DAPI; Thermo Scientific, cat: 62249 were added to each
697 well (1:20,000) in DPBS and incubated with rocking at RT for one hour. Cells were
698 washed 3x2 minutes with DPBS just prior to imaging on the Nikon Ti-2 spinning disk
699 confocal with a 40x oil immersion objective. Images were captured with multiple Z
700 planes to allow visualization of labeled protein colocalization. After acquisition, IMARIS
701 Software (Bitplane, Oxford Instruments, version 9.5.1) and Nikon Elements Analysis
702 software were used to quantify stained proteins. Nuclear pools of proteins were
703 identified using IMARIS software by generating surfaces based on the DAPI channel
704 that represent individual cell nuclei. Mean intensities for all channels within each nuclear
705 surface were exported and analyzed for statistical significance using GraphPad Prism
706 software. Whole cell protein abundance was determined by drawing regions of interest
707 in Nikon Elements Analysis software of single cells. Mean intensities for all channels
708 were exported and analyzed for statistical significance using GraphPad Prism software.
709

710 *Live Cell Staining*

711 H1299, MDA-MB-231, and U-2 OS cells were plated on the pre-prepared synthetic ECM
712 plates 48 hours prior to imaging at 75,000 cells/well in 100 µL solution volume. Images
713 were acquired as outlined in the above sections. Cell nuclei and cell membranes were
714 visualized via Hoechst dye (DAPI; Thermo Scientific, cat: 62249; 1:10,000) and
715 CellMask Deep Red (Thermo Fisher, C10046; 1:20,000), respectively, incubated for 15

716 minutes at 37º C in complete media. Fields of view were selected by visualizing nuclei
717 (DAPI) and images were collected in the DAPI (30% laser power, 600 ms), GFP (30%
718 laser power, 600 ms), Cy5 (30% laser power, 600 ms), and DIC (32.6 DIA, 50 ms)
719 channels. Individual cells were analyzed by IMARIS software by generating cells based
720 on the CellMask channel that represents cell membranes. Cell areas were exported and
721 analyzed for statistical significance using GraphPad Prism software.
722
723 *Single-cell FOXC2 transcriptional activity assay using live-cell microscopy*
724 FOXC2-TAG-Puro expressing H1299 cells were plated on the pre-prepared synthetic
725 ECM plates 48 hours prior to imaging at 75,000 cells/well in 100 µL solution volume.
726 Images were acquired as outlined in the above sections. Cell nuclei and cell
727 membranes were visualized via Hoechst dye (DAPI; Thermo Scientific, cat: 62249;
728 1:10,000) and CellMask Deep Red (Thermo Fisher, C10046; 1:20,000), respectively,
729 incubated for 15 minutes at 37º C in complete media. Fields of view were selected by
730 visualizing nuclei (DAPI) and images were collected in the DAPI (30% laser power, 600
731 ms), GFP (30% laser power, 600 ms), Cy5 (30% laser power, 600 ms), and DIC (32.6
732 DIA, 50 ms) channels. Whole-cell regions of interest (ROIs) were drawn within individual
733 cells using cell mask as a membrane marker and the average GFP intensity for
734 individual cells were exported to Excel. Single-cell intensities were imported to
735 GraphPad Prism for statistical analysis and visualization.
736
737 *BCECF plate reader assays*

738 Cells were plated at 4.0×10^4–8.0×10^4 cells/well in a 24-well plate and incubated
739 overnight. Cells were treated with 2 μM 2′,7′-bis-(2-carboxyethyl)-5-(and-6)-
740 carboxyfluorescein, acetoxymethyl ester (BCECF-AM; VWR, 89139-244) for 20 min at
741 37°C and 5% CO_2. H1299 parental and NHE1 K.O. cells were washed three times for 5
742 min each time with a pre-warmed (37°C) HEPES-based wash buffer (30 mM HEPES pH
743 7.4, 145 mM NaCl, 5 mM KCl, 10 mM glucose, 1 mM $MgSO_4$, 1 mM $KHPO_4$, 2 mM
744 $CaCl_2$, pH 7.4) to match their low bicarbonate medium (RPMI) and NHE1 K.O. Bicarb.
745 cells were washed three times for 5 min each time with a pre-warmed (37°C) HEPES-
746 based wash buffer (30 mM HEPES pH 7.4, 95 mM NaCl, 5 mM KCl, 10 mM glucose, 1
747 mM $MgSO_4$, 1 mM $KHPO_4$, 2 mM $CaCl_2$, pH 7.4) to match sodium bicarbonate
748 treatment. For standardization, three calibration buffers (25 mM HEPES, 105 mM KCl, 1
749 mM $MgCl_2$) were supplemented with 10 μM nigericin (Thermo Fisher Scientific, N1495),
750 pH was adjusted to ~6.7, ~7.0, and ~7.7, and were pre-warmed to 37°C. Fluorescence
751 was read (excitation of 440 and 490 nm, both with emission at 535 nm) on a Cytation 5
752 (BioTek) plate reader incubated at 37°C with 5% CO_2. Kinetic reads were taken at 15-s
753 intervals for 5 min, using a protocol established within BioTek Gen5 software. After the
754 initial pHi read, the HEPES/bicarbonate wash was aspirated and replaced with one of
755 the nigericin buffer standards, and cells were incubated at 37°C with 5% CO_2 for 7 min.
756 BCECF fluorescence was read by the plate reader as above. This process was
757 repeated with the second nigericin standard. As it takes significant time to equilibrate
758 CO_2 in the plate reader, we did not measure nigericin standardizations without CO_2. The
759 mean intensity ratio (490/440 values) was derived from each read. Measurements were

760 calculated from a nigericin linear regression using exact nigericin buffer pH to two
761 decimal places[37].
762
763 *NHE1 Recovery Assay*
764 80,000 cells were plated in the first two rows of a 24-well plate two days prior to
765 transfection (one row of H1299 parental, the other H1299 NHE1 K.O.). Cells were
766 treated with 2 μM 2′,7′-bis-(2-carboxyethyl)-5-(and-6)-carboxyfluorescein, acetoxymethyl
767 ester (BCECF-AM; VWR, 89139-244) for 20 min at 37°C and 5% CO_2. H1299 parental
768 and NHE1 K.O. cells were washed three times for 5 min each time with a pre-warmed
769 (37°C) HEPES-based wash buffer (30 mM HEPES pH 7.4, 145 mM NaCl, 5 mM KCl, 10
770 mM glucose, 1 mM $MgSO_4$, 1 mM $KHPO_4$, 2 mM $CaCl_2$, pH 7.4) to match their low
771 bicarbonate medium (RPMI). Fluorescence was read (excitation of 440 and 490 nm,
772 both with emission at 535 nm) on a Cytation 5 (BioTek) plate reader incubated at 37°C
773 with 5% CO_2. Kinetic reads were taken at ~30 sec intervals for 5 min, using a protocol
774 established within BioTek Gen5 software. Initial baseline images were taken in the
775 HEPES buffer at pH 7.4 (6 mins total). Next, cells were loaded with ammonium chloride
776 using a HEPES-based ammonium chloride buffer (30mM HEPES pH-7.4, 30mM NH_4Cl,
777 115mM NaCl, 5mM KCl, 10mM glucose, 1mM $MgSO_4$, 1mM $KHPO_4$, 2mM $CaCl_2$) and
778 cells were read for 6min. An acid load was induced by removing the ammonium chloride
779 buffer and replacing it with the HEPES buffer (no NH_4Cl). Cells were read while they
780 recovered for 10 minutes. A calibration curve was then obtained by imaging the cells in
781 nigericin containing buffers at the various pH values, around 7.5, 7.0, and 6.5. The
782 standard curve was then used to back calculate the pHi of the cells during the

783 experiment as previously described[35]. The data was normalized to the initial point of the
784 recovery period to look at the recovery rate differences.
785
786 *Statistical analysis*
787 GraphPad Prism was used to prepare graphs and perform statistical analyses. All data
788 sets were subject to normality tests (D'Angostino & Pearson, Anderson-Darling,
789 Shapiro-Wilk, and Kolmogorov-Smirnov) and outlier analyses using the ROUT method
790 (Q=1%). For non-normally distributed data, a Kruskal–Wallis test with Dunn's multiple
791 comparisons correction was used and variance is reported as IQR (Figures 1-6). For
792 fold increase in cell number and population pHi data, one-way ANOVA was used and
793 variance is reported as SEM (Figure 2E, 6A). One-way ANOVA tests assume equal
794 variance while Kruskal- Wallis does not. All significance was indicated in figures by the
795 following: *P<0.05; **P<0.01; ***P<0.001; ****P<0.0001.
796
797 *Replication*
798 We performed 3-6 biological replicates for all cell-based data. Because single-cell
799 imaging is used heavily, we also confirmed pHi manipulation across each replicate
800 included for subsequent VM or molecular marker analyses.
801
802 *Blinding*
803 In addition to the quantitative analysis of vascular mimicry, we blinded imaging data and
804 had other members of the White Lab group/score based on morphology changes. In all

805 cases, White lab members were able to reliably differentiate between soft and stiff
806 matrix but were unable to reliably differentiate soft and "stiff with high pHi" samples.
807
808 *Considering sex as a biological variable*
809 This is not appropriate for this experimental data.
810
811 *Antibodies*
812 Where possible, antibodies were selected from those previously validated by the
813 authors using genetic validation techniques (knock-out of protein of interest, over-
814 expression of protein of interest, selection of cell line that doesn't express protein as
815 true negative control) and independent antibody validation techniques (comparison of
816 staining patterns of two independent antibodies and comparison to literature).
817
818 *Cell Line Authentication*
819 All actively cultured cell lines are tested every 6 months for mycoplasma, and
820 genetically validated through STR Profiling every 5 years. Upon receipt of cells that
821 have not been cultured in the lab, cell lines are tested for mycoplasma and genetically
822 validated through STR Profiling. The White Lab's response to any positive mycoplasma
823 test is to discard any stocks made after the last mycoplasma-free testing. These cells
824 were validated in 2022 and again in Dec 2024. If testing reveals that any of the
825 commercially obtained cell lines (or cell lines from other labs) are misidentified, stocks
826 will be discarded, anyone with whom the stocks were shared will be notified, and source
827 (ATCC or another lab) will be notified.

828

829 **Online Supplementary Materials:** Online supplementary materials include Figure S1-
830 S9.

831

832 **Data and Materials Availability:** All data are available in the main text or the
833 supplementary materials.

834

835 **Acknowledgements:** We like to thank members of the White lab for their helpful
836 conversations and feedback during figure and manuscript preparation. We also thank
837 Dr. Diane Barber for her generous gift of the H1299-NHE1 K.O. cell line. The spinning
838 disk confocal microscope used in this work is a part of the Notre Dame Integrated
839 Imaging Facility (NDIIF).

840

841 **Author contributions:** Conceptualization: LML, KAW, DH-P; Methodology: LML, KAW,
842 LA, KJT, DH-P; Validation: LML, KAW, DH-P; Formal analysis:, LML, LA, LNM, EH, JH,
843 RM, IA, KJT, KAW, DH-P; Investigation: LML, LA, LNM, EH, JH; Resources: KAW, DH-
844 P.; Data collection: LML, LA, LNM, EH, JH, IA, KJT; Data curation: LML, LA, LNM, EH,
845 JH, IA, KJT, KAW, DH-P; Writing – original draft: LML, KAW; Writing - review & editing:
846 LML, LA, LNM, EH, JH, RM, IA, KJT, DH-P; Visualization: LML, LNM, KAW, DH-P;
847 Supervision: KAW, DH-P; Project administration: KAW, DH-P; Funding acquisition:
848 LML, KAW, DH-P.

849

Competing Interests: Authors declare no competing interests.

Funding: This work was supported by the Walther Cancer Foundation Interdisciplinary Interface Training Project (to LML), the Henry Luce Foundation (to KAW), Harper Cancer Research Institute (to KAW & DH-P), an NIH Director's New Innovator Award (1DP2CA260416-01) (to KAW), American Cancer Society Institutional Research Grant (IRG-17-182-04 to DH-P), American Heart Association Career Development Award (19-CDA-34630012 to DH-P), National Institutes of Health (1R35-GM-143055 to DH-P).

References

(1) Walker, C.; Mojares, E.; del Río Hernández, A. Role of Extracellular Matrix in Development and Cancer Progression. *Int. J. Mol. Sci.* **2018**, *19* (10), 3028. https://doi.org/10.3390/ijms19103028.

(2) Carey, S. P.; Martin, K. E.; Reinhart-King, C. A. Three-Dimensional Collagen Matrix Induces a Mechanosensitive Invasive Epithelial Phenotype. *Sci. Rep.* **2017**, *7* (1), 42088. https://doi.org/10.1038/srep42088.

(3) Wechman, S. L.; Emdad, L.; Sarkar, D.; Das, S. K.; Fisher, P. B. Vascular Mimicry: Triggers, Molecular Interactions and in Vivo Models. *Adv. Cancer Res.* **2020**, *148*, 27–67. https://doi.org/10.1016/bs.acr.2020.06.001.

(4) Webb, B. A.; Chimenti, M.; Jacobson, M. P.; Barber, D. L. Dysregulated pH: A Perfect Storm for Cancer Progression. *Nat. Rev. Cancer* **2011**, *11* (9), 671–677. https://doi.org/10.1038/nrc3110.

(5) White, K. A.; Grillo-Hill, B. K.; Barber, D. L. Cancer Cell Behaviors Mediated by Dysregulated pH Dynamics at a Glance. *J. Cell Sci.* **2017**, *130* (4), 663–669. https://doi.org/10.1242/jcs.195297.

(6) Reshkin, S. J.; Greco, M. R.; Cardone, R. A. Role of pHi, and Proton Transporters in Oncogene-Driven Neoplastic Transformation. *Philos. Trans. R. Soc. B Biol. Sci.* **2014**, *369* (1638), 20130100. https://doi.org/10.1098/rstb.2013.0100.

(7) Gilkes, D. M.; Semenza, G. L.; Wirtz, D. Hypoxia and the Extracellular Matrix: Drivers of Tumour Metastasis. *Nat. Rev. Cancer* **2014**, *14* (6), 430–439. https://doi.org/10.1038/nrc3726.

(8) Bordeleau, F.; Mason, B. N.; Lollis, E. M.; Mazzola, M.; Zanotelli, M. R.; Somasegar, S.; Califano, J. P.; Montague, C.; LaValley, D. J.; Huynh, J.; Mencia-Trinchant, N.; Negrón Abril, Y. L.; Hassane, D. C.; Bonassar, L. J.; Butcher, J. T.; Weiss, R. S.; Reinhart-King, C. A. Matrix Stiffening Promotes a Tumor Vasculature Phenotype. *Proc. Natl. Acad. Sci. U. S. A.* **2017**, *114* (3), 492–497. https://doi.org/10.1073/pnas.1613855114.

(9) DuChez, B. J.; Doyle, A. D.; Dimitriadis, E. K.; Yamada, K. M. Durotaxis by Human Cancer Cells. *Biophys. J.* **2019**, *116* (4), 670–683. https://doi.org/10.1016/j.bpj.2019.01.009.
(10) Nallanthighal, S.; Heiserman, J. P.; Cheon, D.-J. The Role of the Extracellular Matrix in Cancer Stemness. *Front. Cell Dev. Biol.* **2019**, *7*, 86. https://doi.org/10.3389/fcell.2019.00086.
(11) Bevensee, M. O.; Boron, W. F. EFFECTS OF ACUTE HYPOXIA ON INTRACELLULAR-pH REGULATION IN ASTROCYTES CULTURED FROM RAT HIPPOCAMPUS. *Brain Res.* **2008**, *1193*, 143–152. https://doi.org/10.1016/j.brainres.2007.12.002.
(12) Burbridge, M. F.; West, D. C.; Atassi, G.; Tucker, G. C. The Effect of Extracellular pH on Angiogenesis in Vitro. *Angiogenesis* **1999**, *3* (3), 281–288. https://doi.org/10.1023/a:1009092511894.
(13) Ulmschneider, B.; Grillo-Hill, B. K.; Benitez, M.; Azimova, D. R.; Barber, D. L.; Nystul, T. G. Increased Intracellular pH Is Necessary for Adult Epithelial and Embryonic Stem Cell Differentiation. *J. Cell Biol.* **2016**, *215* (3), 345–355. https://doi.org/10.1083/jcb.201606042.
(14) Liu, Y.; White, K. A.; Barber, D. L. Intracellular pH Regulates Cancer and Stem Cell Behaviors: A Protein Dynamics Perspective. *Front. Oncol.* **2020**, *10*, 1401. https://doi.org/10.3389/fonc.2020.01401.
(15) Choi, C.-H.; Webb, B. A.; Chimenti, M. S.; Jacobson, M. P.; Barber, D. L. pH Sensing by FAK-His58 Regulates Focal Adhesion Remodeling. *J. Cell Biol.* **2013**, *202* (6), 849–859. https://doi.org/10.1083/jcb.201302131.
(16) Czowski, B. J.; Romero-Moreno, R.; Trull, K. J.; White, K. A. Cancer and pH Dynamics: Transcriptional Regulation, Proteostasis, and the Need for New Molecular Tools. *Cancers* **2020**, *12* (10), 2760. https://doi.org/10.3390/cancers12102760.
(17) Czowski, B. J.; White, K. A. Intracellular pH Regulates β-Catenin with Low pHi Increasing Adhesion and Signaling Functions. March 27, 2024. https://doi.org/10.1101/2024.03.22.586349.
(18) Benton, G.; Arnaoutova, I.; George, J.; Kleinman, H. K.; Koblinski, J. Matrigel: From Discovery and ECM Mimicry to Assays and Models for Cancer Research. *Adv. Drug Deliv. Rev.* **2014**, *79–80*, 3–18. https://doi.org/10.1016/j.addr.2014.06.005.
(19) Kim, P. K.; Halbrook, C. J.; Kerk, S. A.; Radyk, M.; Wisner, S.; Kremer, D. M.; Sajjakulnukit, P.; Andren, A.; Hou, S. W.; Trivedi, A.; Thurston, G.; Anand, A.; Yan, L.; Salamanca-Cardona, L.; Welling, S. D.; Zhang, L.; Pratt, M. R.; Keshari, K. R.; Ying, H.; Lyssiotis, C. A. Hyaluronic Acid Fuels Pancreatic Cancer Cell Growth. *eLife 10*, e62645. https://doi.org/10.7554/eLife.62645.
(20) Deng, B.; Zhao, Z.; Kong, W.; Han, C.; Shen, X.; Zhou, C. Biological Role of Matrix Stiffness in Tumor Growth and Treatment. *J. Transl. Med.* **2022**, *20* (1), 540. https://doi.org/10.1186/s12967-022-03768-y.
(21) Fan, F.; Su, B.; Kolodychak, A.; Ekwueme, E.; Alderfer, L.; Saha, S.; Webber, M. J.; Hanjaya-Putra, D. Hyaluronic Acid Hydrogels with Phototunable Supramolecular Cross-Linking for Spatially Controlled Lymphatic Tube Formation. *ACS Appl. Mater. Interfaces* **2023**, *15* (50), 58181–58195. https://doi.org/10.1021/acsami.3c12514.
(22) Hanjaya-Putra, D.; Yee, J.; Ceci, D.; Truitt, R.; Yee, D.; Gerecht, S. Vascular Endothelial Growth Factor and Substrate Mechanics Regulate in Vitro Tubulogenesis of Endothelial Progenitor Cells. *J. Cell. Mol. Med.* **2010**, *14* (10), 2436–2447. https://doi.org/10.1111/j.1582-4934.2009.00981.x.

(23) Albeiroti, S.; Soroosh, A.; de la Motte, C. A. Hyaluronan's Role in Fibrosis: A Pathogenic Factor or a Passive Player? *BioMed Res. Int.* **2015**, *2015*, e790203. https://doi.org/10.1155/2015/790203.
(24) Nemec, S.; Ganda, S.; Al Taief, K.; Kopecky, C.; Kuchel, R.; Lebhar, H.; Marquis, C. P.; Thordarson, P.; Kilian, K. A. A Tunable Tumor Microenvironment through Recombinant Bacterial Collagen-Hyaluronic Acid Hydrogels. *ACS Appl. Bio Mater.* **2022**. https://doi.org/10.1021/acsabm.2c00186.
(25) Alderfer, L.; Russo, E.; Archilla, A.; Coe, B.; Hanjaya-Putra, D. Matrix Stiffness Primes Lymphatic Tube Formation Directed by Vascular Endothelial Growth Factor-C. *FASEB J. Off. Publ. Fed. Am. Soc. Exp. Biol.* **2021**, *35* (5), e21498. https://doi.org/10.1096/fj.202002426RR.
(26) Piersma, B.; Hayward, M.-K.; Weaver, V. M. Fibrosis and Cancer: A Strained Relationship. *Biochim. Biophys. Acta Rev. Cancer* **2020**, *1873* (2), 188356. https://doi.org/10.1016/j.bbcan.2020.188356.
(27) Cooper, J.; Giancotti, F. G. Integrin Signaling in Cancer: Mechanotransduction, Stemness, Epithelial Plasticity, and Therapeutic Resistance. *Cancer Cell* **2019**, *35* (3), 347–367. https://doi.org/10.1016/j.ccell.2019.01.007.
(28) Gan, Z.; Qin, X.; Liu, H.; Liu, J.; Qin, J. Recent Advances in Defined Hydrogels in Organoid Research. *Bioact. Mater.* **2023**, *28*, 386–401. https://doi.org/10.1016/j.bioactmat.2023.06.004.
(29) Pickup, M. W.; Mouw, J. K.; Weaver, V. M. The Extracellular Matrix Modulates the Hallmarks of Cancer. *EMBO Rep.* **2014**, *15* (12), 1243–1253. https://doi.org/10.15252/embr.201439246.
(30) Vanderhooft, J. L.; Alcoutlabi, M.; Magda, J. J.; Prestwich, G. D. Rheological Properties of Cross-Linked Hyaluronan-Gelatin Hydrogels for Tissue Engineering. *Macromol. Biosci.* **2009**, *9* (1), 20–28. https://doi.org/10.1002/mabi.200800141.
(31) Mammoto, A.; Connor, K. M.; Mammoto, T.; Yung, C. W.; Huh, D.; Aderman, C. M.; Mostoslavsky, G.; Smith, L. E. H.; Ingber, D. E. A Mechanosensitive Transcriptional Mechanism That Controls Angiogenesis. *Nature* **2009**, *457* (7233), 1103–1108. https://doi.org/10.1038/nature07765.
(32) Slater, K.; Partridge, J.; Nandivada, H.; Usa, M. Tuning the Elastic Moduli of Corning® Matrigel® and Collagen I 3D Matrices by Varying the Protein Concentration.
(33) Alderfer, L.; Saha, S.; Fan, F.; Wu, J.; Littlepage, L. E.; Hanjaya-Putra, D. Multi-Parameter Tunable Synthetic Matrix for Engineering Lymphatic Vessels. *Commun. Biol.* **2024**, *7* (1), 1262. https://doi.org/10.1038/s42003-024-06935-7.
(34) Soofi, S. S.; Last, J. A.; Liliensiek, S. J.; Nealey, P. F.; Murphy, C. J. The Elastic Modulus of Matrigel™ as Determined by Atomic Force Microscopy. *J. Struct. Biol.* **2009**, *167* (3), 216–219. https://doi.org/10.1016/j.jsb.2009.05.005.
(35) Spear, J. S.; White, K. A. Single-Cell Intracellular pH Dynamics Regulate the Cell Cycle by Timing the G1 Exit and G2 Transition. *J. Cell Sci.* **2023**, *136* (10), jcs260458. https://doi.org/10.1242/jcs.260458.
(36) Koivusalo, M.; Welch, C.; Hayashi, H.; Scott, C. C.; Kim, M.; Alexander, T.; Touret, N.; Hahn, K. M.; Grinstein, S. Amiloride Inhibits Macropinocytosis by Lowering Submembranous pH and Preventing Rac1 and Cdc42 Signaling. *J. Cell Biol.* **2010**, *188* (4), 547–563. https://doi.org/10.1083/jcb.200908086.

977 (37) Grillo-Hill, B. K.; Webb, B. A.; Barber, D. L. Ratiometric Imaging of pH Probes.
978 *Methods Cell Biol.* **2014**, *123*, 429–448. https://doi.org/10.1016/B978-0-12-420138-5.00023-
979 9.
980 (38) Liu, Y.; Reyes, E.; Castillo-Azofeifa, D.; Klein, O. D.; Nystul, T.; Barber, D. L.
981 Intracellular pH Dynamics Regulates Intestinal Stem Cell Lineage Specification. *Nat.*
982 *Commun.* **2023**, *14* (1), 3745. https://doi.org/10.1038/s41467-023-39312-9.
983 (39) Martin, C.; Pedersen, S. F.; Schwab, A.; Stock, C. Intracellular pH Gradients in
984 Migrating Cells. *Am. J. Physiol.-Cell Physiol.* **2011**, *300* (3), C490–C495.
985 https://doi.org/10.1152/ajpcell.00280.2010.
986 (40) Williamson, S. C.; Metcalf, R. L.; Trapani, F.; Mohan, S.; Antonello, J.; Abbott, B.;
987 Leong, H. S.; Chester, C. P. E.; Simms, N.; Polanski, R.; Nonaka, D.; Priest, L.; Fusi, A.;
988 Carlsson, F.; Carlsson, A.; Hendrix, M. J. C.; Seftor, R. E. B.; Seftor, E. A.; Rothwell, D. G.;
989 Hughes, A.; Hicks, J.; Miller, C.; Kuhn, P.; Brady, G.; Simpson, K. L.; Blackhall, F. H.;
990 Dive, C. Vasculogenic Mimicry in Small Cell Lung Cancer. *Nat. Commun.* **2016**, *7*, 13322.
991 https://doi.org/10.1038/ncomms13322.
992 (41) Racordon, D.; Valdivia, A.; Mingo, G.; Erices, R.; Aravena, R.; Santoro, F.; Bravo, M.
993 L.; Ramirez, C.; Gonzalez, P.; Sandoval, A.; González, A.; Retamal, C.; Kogan, M. J.; Kato,
994 S.; Cuello, M. A.; Osorio, G.; Nualart, F.; Alvares, P.; Gago-Arias, A.; Fabri, D.; Espinoza,
995 I.; Sanchez, B.; Corvalán, A. H.; Pinto, M. P.; Owen, G. I. Structural and Functional
996 Identification of Vasculogenic Mimicry in Vitro. *Sci. Rep.* **2017**, *7* (1), 6985.
997 https://doi.org/10.1038/s41598-017-07622-w.
998 (42) Schnellmann, R.; Ntekoumes, D.; Choudhury, M. I.; Sun, S.; Wei, Z.; Gerecht, S.
999 Stiffening Matrix Induces Age-Mediated Microvascular Phenotype Through Increased Cell
1000 Contractility and Destabilization of Adherens Junctions. *Adv. Sci.* **2022**, *9* (22), 2201483.
1001 https://doi.org/10.1002/advs.202201483.
1002 (43) Delgado-Bellido, D.; Zamudio-Martínez, E.; Fernández-Cortés, M.; Herrera-Campos, A.
1003 B.; Olmedo-Pelayo, J.; Perez, C. J.; Expósito, J.; de Álava, E.; Amaral, A. T.; Valle, F. O.;
1004 Diaz, A. G.; Oliver, F. J. VE-Cadherin Modulates β-Catenin/TCF-4 to Enhance
1005 Vasculogenic Mimicry. *Cell Death Dis.* **2023**, *14* (2), 135. https://doi.org/10.1038/s41419-
1006 023-05666-7.
1007 (44) Qi, L.; Song, W.; Liu, Z.; Zhao, X.; Cao, W.; Sun, B. Wnt3a Promotes the Vasculogenic
1008 Mimicry Formation of Colon Cancer via Wnt/β-Catenin Signaling. *Int. J. Mol. Sci.* **2015**, *16*
1009 (8), 18564–18579. https://doi.org/10.3390/ijms160818564.
1010 (45) Cannell, I. G.; Sawicka, K.; Pearsall, I.; Wild, S. A.; Deighton, L.; Pearsall, S. M.; Lerda,
1011 G.; Joud, F.; Khan, S.; Bruna, A.; Simpson, K. L.; Mulvey, C. M.; Nugent, F.; Qosaj, F.;
1012 Bressan, D.; Dive, C.; Caldas, C.; Hannon, G. J. FOXC2 Promotes Vasculogenic Mimicry
1013 and Resistance to Anti-Angiogenic Therapy. *Cell Rep.* **2023**, *42* (8).
1014 https://doi.org/10.1016/j.celrep.2023.112791.
1015 (46) White, K. A.; Grillo-Hill, B. K.; Esquivel, M.; Peralta, J.; Bui, V. N.; Chire, I.; Barber, D.
1016 L. β-Catenin Is a pH Sensor with Decreased Stability at Higher Intracellular pH. *J. Cell Biol.*
1017 **2018**, *217* (11), 3965–3976. https://doi.org/10.1083/jcb.201712041.
1018 (47) Kisor, K. P.; Ruiz, D. G.; Jacobson, M. P.; Barber, D. L. A Role for pH Dynamics
1019 Regulating Transcription Factor DNA-Binding Selectivity. *Nucleic Acids Res.* **2025**, *53* (10),
1020 gkaf474. https://doi.org/10.1093/nar/gkaf474.
1021 (48) Cha, B.; Geng, X.; Mahamud, M. R.; Fu, J.; Mukherjee, A.; Kim, Y.; Jho, E.-H.; Kim, T.
1022 H.; Kahn, M. L.; Xia, L.; Dixon, J. B.; Chen, H.; Srinivasan, R. S. Mechanotransduction

Activates Canonical Wnt/β-Catenin Signaling to Promote Lymphatic Vascular Patterning and the Development of Lymphatic and Lymphovenous Valves. *Genes Dev.* **2016**, *30* (12), 1454–1469. https://doi.org/10.1101/gad.282400.116.

(49) Koch, S. Regulation of Wnt Signaling by FOX Transcription Factors in Cancer. *Cancers* **2021**, *13* (14), 3446. https://doi.org/10.3390/cancers13143446.

(50) Gozo, M. C.; Aspuria, P.-J.; Cheon, D.-J.; Walts, A. E.; Berel, D.; Miura, N.; Karlan, B. Y.; Orsulic, S. Foxc2 Induces Wnt4 and Bmp4 Expression during Muscle Regeneration and Osteogenesis. *Cell Death Differ.* **2013**, *20* (8), 1031–1042. https://doi.org/10.1038/cdd.2013.34.

(51) Xu, X.; Zhang, Y.; Wang, X.; Li, S.; Tang, L. Substrate Stiffness Drives Epithelial to Mesenchymal Transition and Proliferation through the NEAT1-Wnt/β-Catenin Pathway in Liver Cancer. *Int. J. Mol. Sci.* **2021**, *22* (21), 12066. https://doi.org/10.3390/ijms222112066.

(52) Astudillo, P. Extracellular Matrix Stiffness and Wnt/β-Catenin Signaling in Physiology and Disease. *Biochem. Soc. Trans.* **2020**, *48* (3), 1187–1198. https://doi.org/10.1042/BST20200026.

(53) Sun, M.; Chi, G.; Xu, J.; Tan, Y.; Xu, J.; Lv, S.; Xu, Z.; Xia, Y.; Li, L.; Li, Y. Extracellular Matrix Stiffness Controls Osteogenic Differentiation of Mesenchymal Stem Cells Mediated by Integrin A5. *Stem Cell Res. Ther.* **2018**, *9* (1), 52. https://doi.org/10.1186/s13287-018-0798-0.

(54) al, J. L. et. *Wnt/β-catenin signalling: function, biological mechanisms, and therapeutic opportunities | EndNote Click*. https://click.endnote.com/viewer?doi=10.1038%2Fs41392-021-00762-6&token=WzIxODg0NzgsIjEwLjEwMzgvczQxMzkyLTAyMS0wMDc2Mi02Il0.6vbvIy-yR3ICpP2WVTCjsQ-z3Z0 (accessed 2025-05-19).

(55) Grillo-Hill, B. K.; Choi, C.; Jimenez-Vidal, M.; Barber, D. L. Increased H+ Efflux Is Sufficient to Induce Dysplasia and Necessary for Viability with Oncogene Expression. *eLife* **2015**, *4*, e03270. https://doi.org/10.7554/eLife.03270.

(56) Amith, S. R.; Wilkinson, J. M.; Fliegel, L. Assessing Na+/H+ Exchange and Cell Effector Functionality in Metastatic Breast Cancer. *Biochim. Open* **2016**, *2*, 16–23. https://doi.org/10.1016/j.biopen.2016.01.001.

(57) Hulikova, A.; Harris, A. L.; Vaughan-Jones, R. D.; Swietach, P. Regulation of Intracellular pH in Cancer Cell Lines under Normoxia and Hypoxia. *J. Cell. Physiol.* **2013**, *228* (4), 743–752. https://doi.org/10.1002/jcp.24221.

(58) Konen, J.; Summerbell, E.; Dwivedi, B.; Galior, K.; Hou, Y.; Rusnak, L.; Chen, A.; Saltz, J.; Zhou, W.; Boise, L. H.; Vertino, P.; Cooper, L.; Salaita, K.; Kowalski, J.; Marcus, A. I. Image-Guided Genomics of Phenotypically Heterogeneous Populations Reveals Vascular Signalling during Symbiotic Collective Cancer Invasion. *Nat. Commun.* **2017**, *8*, 15078. https://doi.org/10.1038/ncomms15078.

(59) Andersen, A. P.; Flinck, M.; Oernbo, E. K.; Pedersen, N. B.; Viuff, B. M.; Pedersen, S. F. Roles of Acid-Extruding Ion Transporters in Regulation of Breast Cancer Cell Growth in a 3-Dimensional Microenvironment. *Mol. Cancer* **2016**, *15* (1), 45. https://doi.org/10.1186/s12943-016-0528-0.